Pure Appl. Geophys. 175 (2018), 4275–4288

https://doi.org/10.1007/s00024-018-1948-0

Pure and Applied Geophysics

A NE-Trending Oblique-Slip Fault Responsible for the 2016 Zaduo Earthquake (Qinghai, China) Revealed by InSAR Data

Guoyan Jiang,[1,5] Yangmao Wen,[2] Kang Li,[3] Lihua Fang,[4] Caijun Xu,[2] Yong Zhang,[2] and Xiwei Xu[3]

Abstract—Twelve Sentinel-1 images are used to measure the surface displacements caused by the Zaduo earthquake on 17 October 2016 in Qinghai, China. Comprehensive analysis of the local geologic structure, focal mechanisms, relocated aftershocks, and fault geometrical parameters from nonlinear inversions of the InSAR data indicates that a NE-trending fault with a strike of ~ 61°, namely the Aduo fault, was responsible for this event. Further geodetic inversions for finite fault models show that the dip angle of this fault is 75° to the SE. The majority of the slip occurred at the depth from 5 km to 17 km, and the normal-slip component was comparable to the strike-slip component. The peak slip of ~ 31 cm occurred at a depth of ~ 10 km. The InSAR determined moment is 9.61×10^{17} N m with a rigidity of 30 GPa, equivalent to Mw 5.9. The geological map reveals that the Aduo fault was characterized by a left-lateral strike-slip component in the past, as evidenced by the offset of Paleogene sedimentary rocks. Our results for the Zaduo earthquake suggest that the Qiangtang block probably consists of two or more sub-blocks with different eastward extrusion velocities and that the deformation of the Qiangtang block is occurring not only along its boundaries but also in its interior.

Key words: The 2016 Zaduo earthquake, InSAR, seismogenic fault, slip distribution, Qiangtang block.

1. Introduction

On 17 October 2016, a moderate earthquake with a moment magnitude of approximately 6 occurred in the Qiangtang block, Tibet Plateau, approximately 35 km from Zaduo city in Qinghai province (Fig. 1). The hypocenter depths reported by different agencies vary from 9.0 to 30.5 km (Table 1). The USGS W-phase moment tensor solutions suggest a predominantly normal-faulting event. In contrast, the results from the Global Centroid Moment Tensor project (GCMT) (Dziewonski et al. 1981; Ekström et al. 2012) and the Institute of Geophysics of China Earthquake Administration (IGPCEA) give moment tensor solutions suggesting that the strike-slip component was comparable to the normal-slip component. These discrepancies raise questions about the determination of the location, strike, dip and rake of the causative fault, which did not rupture to the surface.

Strike-slip faults are widely distributed in the study region surrounding the location of the Zaduo earthquake (Fig. 1). As evidenced by the horizontal GPS velocities in this seismically active region (Liang et al. 2013), these faults play a significant role in the eastward extrusion of the Qiangtang block, which is due to the post-collisional convergence between the Eurasian and Indian plates (e.g., Deng et al. 1979; Tapponier and Molnar 1977). The Jiali and Ganzi–Yushu faults are the southern and northern boundaries of the Qiangtang block, respectively. The latest devastating earthquake on the Ganzi–Yushu fault occurred in 2010 and had a magnitude of M_w 6.9, resulting in more than 2000 deaths (Jiang et al. 2013). The active tectonic map of China shows that there are two faults, one trending NE and one

Electronic supplementary material The online version of this article (https://doi.org/10.1007/s00024-018-1948-0) contains supplementary material, which is available to authorized users.

[1] Collaborative Innovation Center of Geospatial Technology, Wuhan University, Wuhan, China.
[2] School of Geodesy and Geomatics, Wuhan University, Wuhan, China. E-mail: ymwen@sgg.whu.edu.cn
[3] Key Laboratory of Active Tectonics and Volcano, Institute of Geology, China Earthquake Administration, Beijing, China.
[4] Institute of Geophysics, China Earthquake Administration, Beijing, China.
[5] *Present Address*: Earth System Science Programme, The Chinese University of Hong Kong, Hong Kong, China.

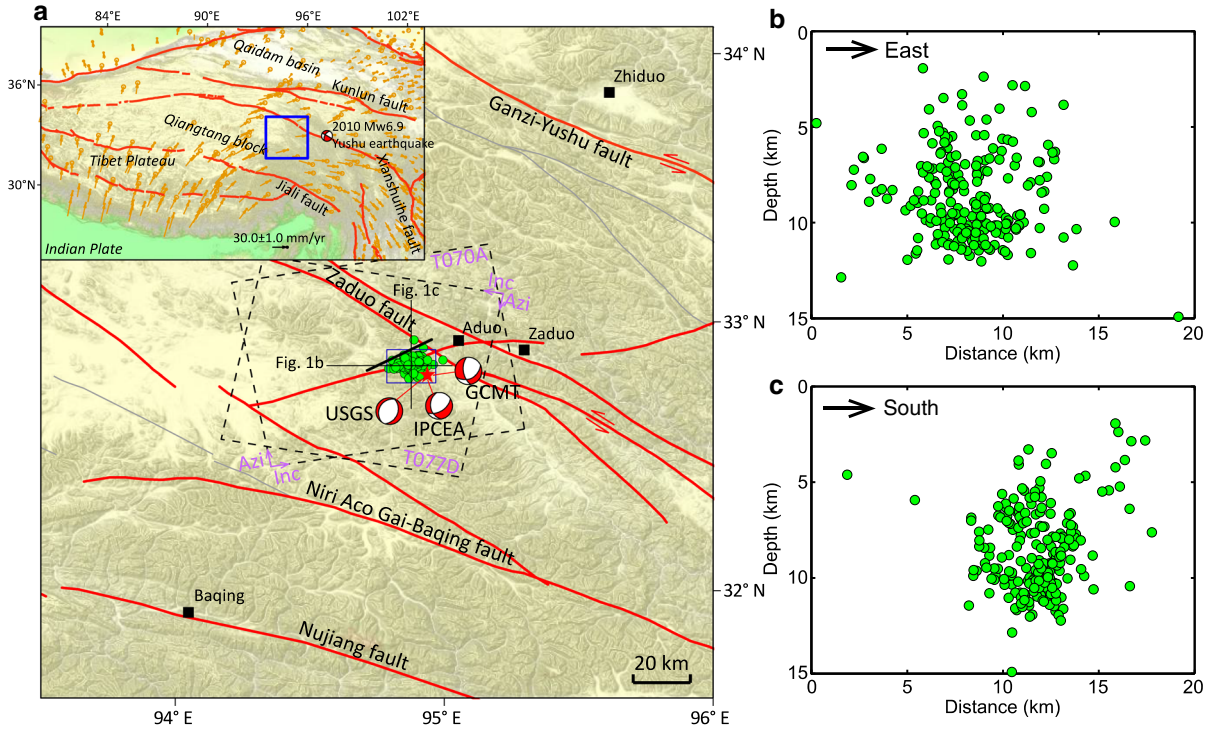

Figure 1

a Tectonic setting of the 17 October 2016 Zaduo earthquake. Red lines are the major faults in the seismic region from the active tectonic map of China (Deng et al. 2007). The black line is the surface trace of the modeled ruptured fault in this study. The green circles are the relocated aftershocks up to 26 November 2016. The red star denotes the relocated hypocenter. The two black dashed rectangles outline the coverage of the ascending and descending InSAR data. **b**, **c** are the depth profiles of the relocated aftershocks in the eastward and southward directions, respectively. The inset map shows the location of the Zaduo earthquake in the Tibetan Plateau, along with major faults. The yellow arrows with error ellipses of 95% confidence are the interseismic GPS velocities (Liang et al. 2013)

Table 1

Reported focal parameters of the 2016 Zaduo earthquake

Source	Nodal plane I (°)			Nodal plane II (°)			Depth (km)	Magnitude
	Strike	Dip	Rake	Strike	Dip	Rake		
USGS	214	40	− 79	20	51	− 99	30.5	M_w 5.9
GCMT	63	59	− 33	171	62	− 145	20.9	M_w 6.0
IGPCEA[a]	58	65	− 45	171	50	− 146	9.0	M_s 6.2
This study	61	75	− 38[b]				~ 10.0[c]	M_w 5.9

[a]http://www.cea-igp.ac.cn/tpxw/274960.html

[b]The rake angle of the maximum slip

[c]The depth of the maximum slip

trending NW, close to the 2016 Zaduo event (Fig. 1a) (Deng et al. 2007). The NW-trending fault is the Zaduo fault. Although both faults were active in the Quaternary, their activity since the late Pleistocene remains unclear. The 2016 earthquake provides an opportunity to identify the activity and faulting mechanism in this region.

Recognition of the seismogenic fault is helpful in understanding the tectonic motion in the center of the Qiangtang block, where GPS stations are sparse. In this study, we first use the ascending and descending Sentinel-1 SAR interferograms to measure the ground displacements caused by the 2016 Zaduo event. Then, together with the local geological structure map, focal mechanisms, and relocated aftershocks, we investigate the fault responsible for the Zaduo earthquake through nonlinear inversions. Furthermore, we conduct linear geodetic inversions to constrain fault dip angle and coseismic slip distribution at depth. Finally, we discuss the implications of the 2016 Zaduo earthquake for the tectonic deformation in the Qiangtang block.

2. *InSAR Observations*

Interferometric synthetic aperture radar (InSAR) observations are widely used to measure the surface displacements associated with geological, tectonic and anthropogenic activities, such as earthquakes, volcanoes, groundwater extraction, and CO_2 geological storage (CGS), especially in the regions without enough global navigation satellite system (GNSS) observation sites (e.g., Bell et al. 2008; Hooper et al. 2004; Jiang et al. 2013). Here, we use six ascending (T070A) and six descending (T077D) Sentinel-1 Terrain Observation with Progressive Scans (TOPS) mode SAR images acquired before and after the 2016 Zaduo earthquake to measure the coseismic surface displacements with the two-pass differential InSAR (DInSAR) technique (Massonnet et al. 1993) (Table 2).

Twelve single look complex (SLC) images are processed into interferograms with GAMMA software (Werner et al. 2001). For TOPS interferometry, a method that considers geometric alignment and spectral diversity (Scheiber and Moreira 2000) is used to ensure an accuracy of a few thousandths of a pixel coregistration in the azimuth direction and to avoid phase jumps between subsequent bursts. The effects of topography are removed from the six interferograms using the precise orbit data provided by European Space Agency (ESA) together with the 90-m resolution Shuttle Radar Topography Mission (SRTM) digital elevation model (DEM) (Farr et al. 2000). Then, the effect of phase noise in our interferograms is reduced using the power spectrum filter (Goldstein and Werner 1998). Finally, the interferograms are unwrapped using the branch-cut method (Goldstein et al. 1988) and geocoded to the WGS84 geographic coordinates with a resolution of 90 m.

The geocoded interferograms (Fig. S1) exhibit some noises due to atmospheric effects, especially in mountain areas. The atmospheric delays of comparable magnitude can be ignored when dealing with medium-to-large earthquakes with strong ground motion but become important when modeling small and/or deeply buried earthquakes with small surface displacements. To overcome this issue, the Generic Atmospheric Correction Online Service (GACOS) (Yu et al. 2017) was used to properly mitigate the topographic-related tropospheric delays by applying the iterative tropospheric decomposition (ITD) method to separate stratified and turbulent signals from tropospheric total delays with high-resolution European Centre for Medium-Range Weather Forecasts (ECMWF) model. GACOS seems to capture the first-order atmospheric effects in the interferograms (Fig. S2), especially for the descending track T077D. After the correction, the average-phase standard deviation (StdDev) (excluding the near-field coseismic region) decreases from 0.53 to 0.50 cm for the ascending track and from 0.48 to 0.36 cm for the descending track.

In addition, assuming that the residual atmospheric noise is temporally random, the signal-to-noise ratios of InSAR coseismic interferograms in both ascending and descending tracks can be increased through multi-interferogram stacking. Figure 2a, b shows the final stacking coseismic interferograms. The subsequent 1D covariance function estimation in Sect. 3.2 reveals that the StdDev values for the ascending and descending tracks decrease to 0.34 and 0.23 cm, respectively.

By combining the ascending and descending interferograms, 2.5-dimensional (2.5D) analysis (Fujiwara et al. 2000; Wen et al. 2016) was conducted to derive displacement maps in both quasi-eastward and quasi-upward components from the line-of-sight (LOS) observations. The LOS displacements (d_{LOS})

Table 2

Information of the InSAR interferograms used in the study

Track	#	Master	Slave	Perpendicular baseline	Incidence angle	Azimuth angle	σ^a	α^b	RMS misfit[c] (cm)	
		DD/MM/YYYY	DD/MM/YYYY	(*m*)	(°)	(°)	(cm)	(km)	NE distributed slip model	NW distributed slip model
T070A	IP1	12/08/2016	10/12/2016	58	39.6	− 10.2	0.34	5.8	0.32	0.36
	IP2	05/09/2016	16/11/2016	− 6						
	IP3	29/09/2016	23/10/2016	− 76						
T077D	IP4	31/07/2016	04/12/2016	19	34.3	− 169.3	0.23	2.8	0.22	0.36
	IP5	24/08/2016	10/11/2016	17						
	IP6	17/09/2016	17/10/2016	− 32						

[a]The standard deviation calculated from 1D covariance function for the stacking deformation

[b]The e-folding correlation length scale of 1D covariance function for the stacking deformation

[c]The root-mean-square (RMS) fitting residuals to the observations

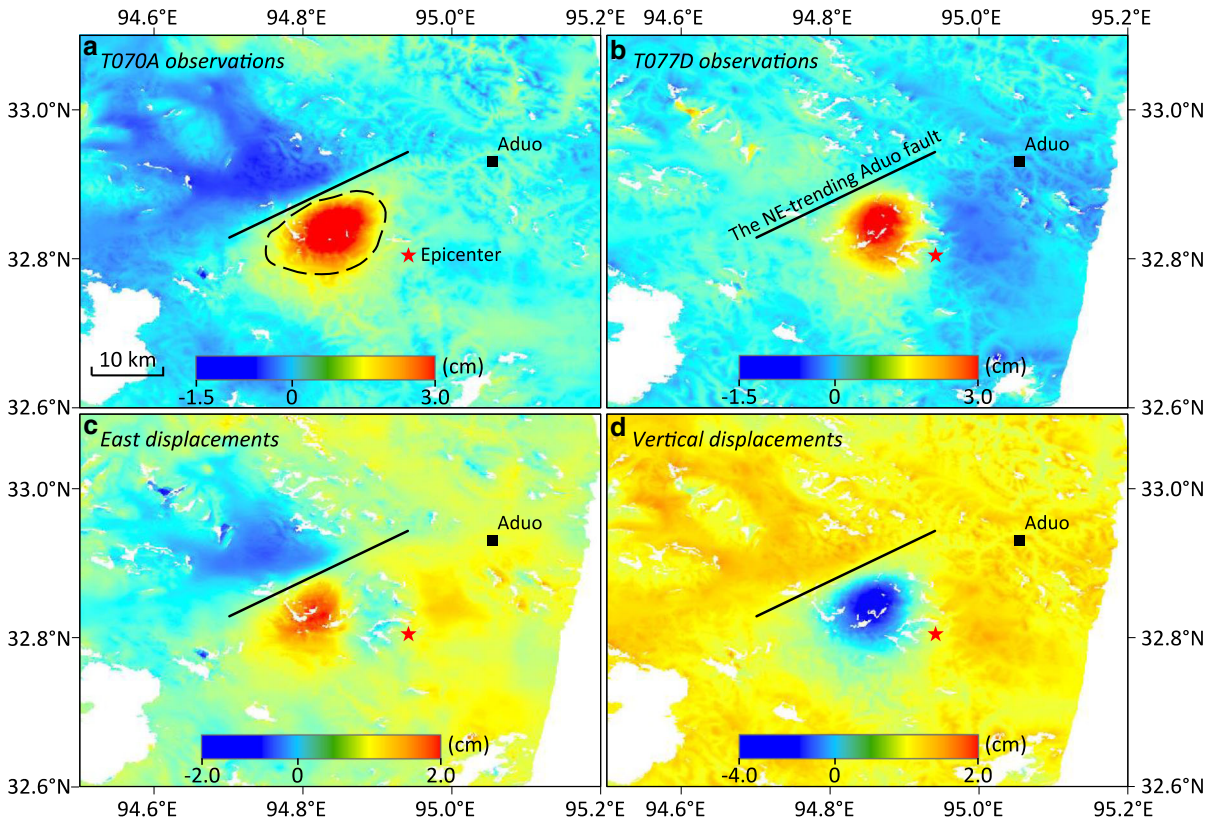

Figure 2

InSAR observations used in this study. **a**, **b** are the two stacking LOS coseismic displacement maps from tracks T070A and T077D, respectively. The color red indicates ground motion away from the satellite. **c**, **d** are the displacement maps in the quasi-eastward and upward directions derived from the ascending and descending InSAR interferograms. The black dashed line outlines the major displacement region

are related with the east (d_e), north (d_n), and vertical (d_u) displacement components through

$$d_{LOS} = d_e \cos\phi \sin\theta + d_n \sin\phi \sin\theta + d_u \cos\theta, \quad (1)$$

where ϕ and θ are the azimuth of the orbit and the incidence angle, respectively. Due to the near-polar orbital geometry (i.e., satellite azimuthal direction is approximately parallel to the north–south orientation), the contribution from the north component to the LOS displacements can be neglected considering the very small value of $\sin\phi$. Therefore, the LOS displacements are approximately equal to $d_e \cos\phi \sin\theta + d_u \cos\theta$. With the ascending and descending InSAR interferograms (Fig. 2a, b), the quasi-eastward and vertical displacement maps can be directly estimated (Fig. 2c, d).

The displacement maps (Fig. 2) reveal that there are two lobes with opposite ground motion. The major displacement signals are confined to an elliptical region of $\sim$ 120 km^2, close to the hypocenter, where subsidence is apparent in the quasi-vertical displacement map (Fig. 2d). In contrast, lower magnitude uplift is observed in the north of the fault trace. This coseismic deformation pattern is similar to the 2008 Dangxiong earthquake, a M_w 6.3 normal-faulting event in southern Tibet (Liu et al. 2012; Xu et al. 2016). Our InSAR observations indicate that the Zaduo earthquake probably has a considerable normal-slip component (Resor 2003).

3. The Seismogenic Fault

Recognition of the seismogenic fault is the basis for further investigations into topics such as rupture processes and dynamics, co- and post-seismic slip models, and stress perturbation. The causative fault can be determined by geologic or geophysical methods. The geologic method is straightforward for continental earthquakes with surface rupturing (e.g., Xu et al. 2006), as well as for some interplate earthquakes (e.g., Fujiwara et al. 2011; Avouac et al. 2015). The geophysical method identifies the causative fault through seismic or geodetic inversions, as well as sometimes using relocated aftershocks (e.g., Fang et al. 2015; Wen et al. 2016). This method is suitable for continental earthquakes without surface rupturing. To explore the deep structures associated with large earthquakes, both the geologic and geophysical methods are often employed simultaneously (e.g., Xu et al. 2009a, b).

For the 2016 Zaduo earthquake, three reported focal mechanism solutions exhibit two different rupture possibilities: normal slip vs. oblique slip (Table 1). The active tectonic map of China reveals two faults near the epicenter, the NW-trending Zaduo fault and an unnamed NE-trending fault (Fig. 1). The NE-trending fault passes through the county of Aduo. Therefore, we refer to this structure as the Aduo fault. The tectonic map shows the Zaduo fault has both strike-slip and reverse-slip components. However, the slip sense of the Aduo fault is unknown. Based only on the seismological solutions, we cannot identify the fault responsible for the earthquake. Therefore, we relocated the aftershocks that occurred during the 40 days following the earthquake and carried out nonlinear geodetic inversions to determine the ruptured fault geometry.

3.1. Relocated Aftershocks

By the end of 26 November 2016, 1047 aftershocks were recorded by the Qinghai Seismic Network (http://www.csi.ac.cn/manage/eqDown/18NPMF/gctw/tzfb/A01.JPG, last accessed 1 November 2017). Among them, 685 aftershocks were recorded by only one station. Their initial event locations were determined using Hypo 2000 (Klein 2002) with the CRUST1.0 velocity model in the source region (Laske et al. 2013). Then, the aftershocks that had at least six phase arrival times and were recorded by more than four stations were relocated with the double-difference algorithm (Waldhauser and Ellsworth 2000), resulting in a total of 225 aftershocks (Fig. 1).

Most of the relocated aftershocks occurred in a 13-km (east–west) $\times$ 11-km (north–south) rectangular region, above a depth of 15 km. The location accuracy of each aftershock is listed in the supplementary data. From the spatial distribution of the aftershocks, we cannot determine a predominant rupture direction. In addition, no information on the fault dip can be obtained from the depth profiles in either the eastward or southward directions (Fig. 1b,

c). Thus, it is still difficult to identify the source fault of the 2016 Zaduo earthquake based on the relocated aftershocks.

3.2. Nonlinear Fault Geometry Estimation with Uniform Slip

To determine the fault geometry, we invert the InSAR measurements with a nonlinear procedure, assuming a uniform slip model. First, the two LOS displacement fields are down-sampled by the quadtree algorithm to reduce the number of observations and the spatial correlation and to weigh the observations in the region with large displacements (Jónsson et al. 2002; Welstead 1999). A total of 417 and 359 observations are obtained from the T070A and T077D interferograms, respectively.

Second, residual spatially correlated signals in the two InSAR interferograms (Fig. 2a, b), primarily attributable to residual atmospheric and ionospheric structures, are estimated using a 1D covariance function in the non-deforming areas (Hanssen 2001),

$$C_{jk} = \sigma^2 e^{-\frac{r_{jk}}{\alpha}}, \tag{2}$$

where C_{jk} and r_{jk} are the covariance and distance between pixels j and k, and σ and α represent the standard deviation and e-folding wavelength (Fig. S3). The standard deviations for tracks T070A and T077D are 0.34 and 0.23 cm, respectively (Table 2), which reveal that our InSAR observations are in a low noise level. These two values are taken as the observation errors of InSAR data for subsequent uncertainty estimation of the fault geometry and slip parameters.

Third, because the two InSAR interferograms have different standard deviations, the optimal weight ratio between them is determined by the Helmert variance component estimation (HVCE) method (Xu et al. 2009a, b), which has various advantages over other methods, especially when the observations are abundant. The optimal weight ratio between the down-sampled T070A and T077D observations is 0.395.

Finally, a global hybrid minimization algorithm based on multi-peak particle swarm optimization (M-PSO) is adopted to determine the fault parameters (Feng et al. 2013), including location, strike, dip, length, depth, width and slip (Table 3), by minimizing the misfits between the observed and the predicted surface displacements based on the classic elastic half-space dislocation model (Okada 1992). Meanwhile, a Monte Carlo test is conducted based on the method described in Parsons et al. (2006) to estimate the uncertainties and trade-offs in the fault geometry parameters. During the test, a full variance–covariance matrix, $\mathbf{\Sigma}$, for the down-sampled observations was generated using the two-fitted 1D covariance functions of both ascending and descending tracks (Eq. 2). A vector of spatially correlated noise, $\mathbf{y}$, can be calculated from a vector of Gaussian uncorrelated noise, $\mathbf{x}$, with a mean of zero and a standard deviation of 1 by

$$\mathbf{y} = \mathbf{L}\mathbf{x}, \tag{3}$$

where $\mathbf{L}$ is the Cholesky decomposition of the variance–covariance matrix (Rubinstein 1981), $\mathbf{\Sigma} = \mathbf{L}\mathbf{L}^{\mathbf{T}}$. The correlated noise is then added back to the original data vector to produce a new noisy data set. The procedure was repeated 100 times to obtain an ensemble of noisy data sets. Finally, each of these noisy data sets is then used in the non-linear inversion procedure to produce a set of model parameters.

The distribution of these model parameters (Fig. S4) can be used to estimate their uncertainties (Table 3). Overall, the estimating results show that the uncertainties are small, which indicates a good confidence of non-linear fault geometry estimation. Several parameters have strong trade-offs, such as between slip and width, and between width and the minimum depth of faulting. The optimization results show that the ruptured fault has a NE strike and is centered at 32.875°N, 94.865°E. The slip magnitude is 38 ± 7 cm, and the strike-slip component is comparable to the dip slip (Table 3).

The center of the best-fit model fault is approximately 2.5 km from the existing NE-trending Aduo fault based on the active tectonic map of China (Deng et al. 2007). The relocated aftershocks locate in the hanging wall of the fault (Fig. 1). The offset between the relocated aftershocks and the modeled fault may be due to three reasons: (1) the use of different crust models in the aftershock relocation and nonlinear inversions; (2) model simplification of a potentially

Table 3

Fault parameters of the Zaduo earthquake derived from nonlinear inversions

Fault center		Depth (km)	Length (km)	Width (km)	Strike (°)	Dip (°)	Rake (°)	Slip	M_w
Longitude (°)	Latitude (°)								
94.865 ± 0.002 km	32.875 ± 0.001 km	8.8 ± 0.2	6.0 ± 0.6	8.7 ± 1.1	61.2 ± 1.9	58.7 ± 2.0	− 39.0 ± 2.2	38 ± 7	5.83

curved seismogenic fault as a linear fault; and/or (3) the modeled fault is the surface trace of the ruptured fault, but the aftershock distribution is a result of horizontal projection. We speculate that the NE-trending Aduo fault is responsible for the 2016 Zaduo earthquake. The existing Aduo fault was first mapped in the 1990s. The offset between the existing and modeled faults may be caused by two factors: (1) model simplification of the ruptured fault in this study, and (2) the low spatial accuracy of the 1:500,000 geological map (Zhang and Zheng 1994) and the low resolution of the aerial photos that were used for active fault mapping.

4. Finite Fault Slip Model

To obtain the rupture model of the Zaduo earthquake, we adopt the same inversion scheme as Jiang et al. (2015) with the modified Laplacian operator. The function model used in the linear inversions for slip models can be formulated as follows:

$$\begin{pmatrix} \boldsymbol{d} \\ 0 \end{pmatrix} = \begin{pmatrix} \boldsymbol{G} & \boldsymbol{L} \\ k\nabla^2 & 0 \end{pmatrix} \begin{pmatrix} \boldsymbol{m} \\ \boldsymbol{s} \end{pmatrix}, \tag{4}$$

where $\boldsymbol{d}$ is the observation vector, $\boldsymbol{m}$ is the slip vector, $\boldsymbol{G}$ is Green's function matrix, ∇^2 is the modified Laplacian operator, and k is the smoothing factor. In addition, an overall linear offset $\boldsymbol{Ls}$ may exist between the InSAR observations and the model result $\boldsymbol{Gm}$, which is primarily attributed to the residual orbit error.

The seismogenic fault from the nonlinear inversions is extended to a width of 25 km, and modeled with 1 km × 1 km rectangular dislocation patches to obtain fine-scale slip features. The elastic half-space dislocation model (Okada 1992) is also used to calculate the Green's function between slip on the patches and the down-sampled InSAR observations. Then, finite fault models are inverted by the bounded variable least-squares algorithm (Stark and Parker 1995) with parameter bounds for both the strike- and dip-slip components.

The fault dip angle of ∼ 59° obtained from the nonlinear optimization is based on the uniform slip model. However, it is probably not appropriate for distributed slip models (Bürgmann et al. 2002; Feng et al. 2013; Fukahata and Wright 2008; Wen et al. 2016). We evaluate this value through inversions with fault models involving variable dip angles. The slip models should not over- or under-fit the InSAR observations. Here, we adopted the normalized root-mean-square (NRMS) as the fitting criteria proposed by McCaffrey (2005):

$$\mathrm{NRMS} = \left[N^{-1} \left(\sum_{i=1}^{N} r_i^2 / \sigma_i^2 \right) \right]^{1/2}, \tag{5}$$

where r is the residual, σ is the datum standard error, and N is the number of observations. The NRMS should be near unity when the model fits the observations well, indicating that the RMS misfit should be close to the observation error. The smoothing constant is fixed at 0.1. The fitting results show that, when the dip angle is equal to 75°, the RMS fitting residuals are in agreement with the estimated InSAR errors (Table 2). The dip angles (45°–60°) with the least misfit of 0.24 cm are not chosen due to some overfitting. More inversions are carried out with the re-determined fault dip to seek a preferred smoothing factor k from the trade-off curve (Fig. 3b), which balances roughness of slip distribution and misfit to the InSAR observations (Jiang et al. 2013).

Our best-fit finite fault model shows that most of the coseismic slip occurred at depths of 5 km to 17 km (Fig. 4a). The peak slip of ∼ 31 cm occurred

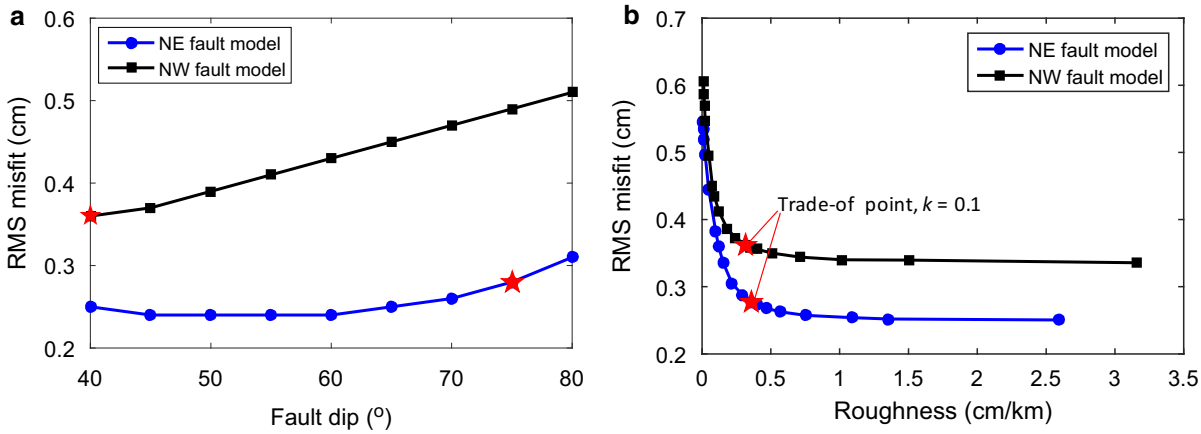

Figure 3
Determination of the optimal dip angles and the preferred smoothing factors for the NE- and NW-trending fault models. **a** Variation of the RMS misfits to InSAR observations with increasing fault dip angles. **b** Trade-off curves between the model residuals and the roughness of the slip models. Red stars denote the selected values in our study

at a depth of ~ 10 km. The released moment was 9.61×10^{17} N m, equivalent to Mw 5.9 with a rigidity of 30 GPa, which is equal to the USGS magnitude. The slip robustness is estimated using the Monte Carlo method to invert the 100 perturbed InSAR data sets above (Fig. 4b). All the uncertainties are less than 1.0 cm with 95% confidence. The predicted LOS displacements and the residuals of both the ascending track T070A and the descending track T077D are shown in Fig. 5. No significant residual signals remain in the vicinity of the seismogenic fault. The RMS fitting residuals of our model to the tracks T070A and T077D interferograms are equal to the standard deviations (Table 2), which indicates that the NRMS value is close to 1.

Compared with the uniform slip model, there are some differences in the slip magnitude, rake, dip and released moment. The maximum slip with rake of the distributed model, listed in Table 1, indicates that the Zaduo earthquake was characterized by oblique slip. The difference in fault dip is attributed to the model assumptions and the inversion schemes. Similar differences are also present in other earthquake models, such as the 12 November 1999 Düzce earthquake in Turkey (Bürgmann et al. 2002) and the June 2004 Tabuk earthquake in Saudi Arabia (Xu et al. 2015). Small differences in the moment magnitudes are also common in many published studies (e.g., Bürgmann et al. 2002; Funning et al. 2005; Parsons et al. 2006; Wen et al. 2016).

5. *Discussion*

To further test the possibility of the NW-trending causative fault with a strike of 128°, we implemented additional inversions to obtain a finite fault model for the NW-trending Zaduo fault with the same InSAR observations and methods. The width of the Zaduo fault was set to 35 km. We also analyzed the influence of different dip angles on the misfits between the observed and the predicted LOS displacements, under a fixed smoothing factor of 0.1. With the dip angle varying from 80° to 40°, the misfit decreases from 0.51 cm to 0.36 cm. The preferred smoothing factor for the NW-trending distributed slip model was also redetermined from the trade-off curve (Fig. 3b), which is consistent with the value selected for the NE-trending distributed slip model.

The resulting slip model shows that major coseismic rupture occurred at depths from 7 to 17 km, with a maximum slip of ~ 22 cm (Fig. 4c). The corresponding seismic moment was 1.09×10^{18} N m, equivalent to Mw 6.0 with a rigidity of 30 GPa. The model uncertainties are still estimated using the Monte Carlo method as above. The InSAR fitting

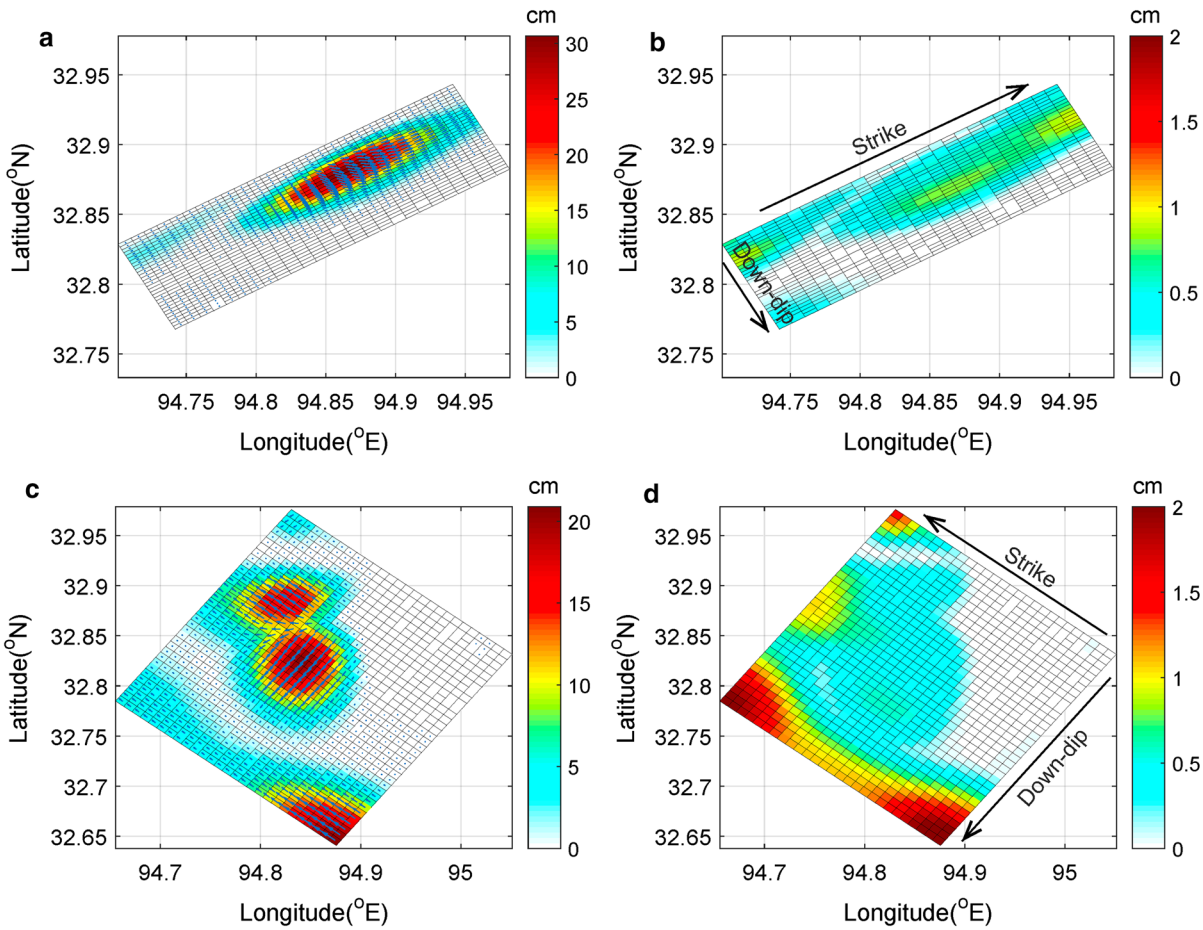

Figure 4
Finite fault slip models derived from InSAR observations. **a**, **c** are the distributed slip distributions of the Zaduo earthquake on the NE- and NW-trending fault planes, respectively. The blue arrows show the slip direction on the fault planes. **b**, **d** are the model uncertainties determined by the Monte Carlo method

results, unlike the InSAR residuals of the NE-trending slip model (Fig. 5), exhibit distinct displacement signals remaining in the residual maps (Fig. 6). The maximum predicted LOS displacement is 2.1 cm, only half of the largest measured value (4.2 cm) in the T070D interferogram. The RMS misfit of the NW-trending model to the T077A interferogram is close to the value of the NE-trending model (Table 2). However, for the T070D interferogram, the misfit of the NW-trending model exceeds the standard deviation by nearly 50%.

The poor fit of the NW-trending model to the InSAR observations also confirms that the NE-trending Aduo fault is responsible for the 2016 Zaduo earthquake. From the 1:500,000 geologic map of Qinghai province (Fig. 7), a distinct fault trace with left-laterally offset strata and a length of up to ~ 60 km emerges to the north of the modeled fault. The distance between the trace and the modeled fault ranges from 0 km to 5.5 km, which may also be caused by our model simplification and the large scale of the geological map. The Paleogene sedimentary rocks have been offset by approximately 8–10 km along the fault, which indicates that the fault was probably characterized with a sinistral strike-slip component. Nevertheless, we are not sure whether this fault also experienced normal slip. Our geodetic inversion results for the Zaduo earthquake

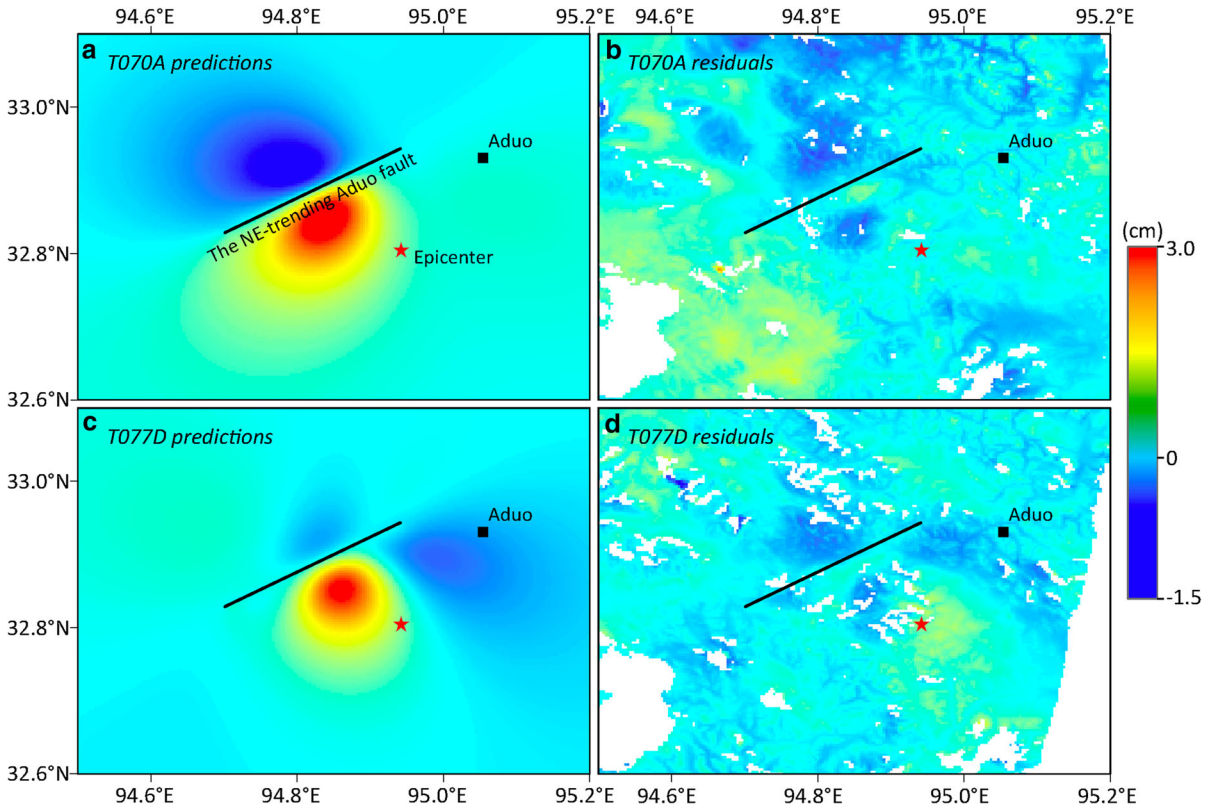

Figure 5
Fitting results of the NE-trending slip model to the two InSAR interferograms. **a**, **c** are the predicted LOS displacement maps for tracks T070A and T077D, respectively. **b**, **d** are the corresponding residual displacements

reveals that the current normal slip on the Aduo fault is not less than the strike slip. If the slip sense of the Aduo fault changed from strike-slip to oblique-slip, it was probably caused by the tectonic transition of the Tibetan Plateau from N–S compression to E–W extension in the late Tertiary to Quaternary, approximately 5 million years ago (England and Houseman 1989). The plateau has been thinning via an extensional mechanism along many approximately N–S-trending normal faults.

The normal-faulting feature of the Zaduo earthquake implies that the Qiangtang block probably consists of two or more sub-blocks with different eastward extrusion velocities. The eastward velocity of the hanging-wall block is faster than the velocity of the foot-wall block, which is probably the direct cause for the Zaduo earthquake. The NW-trending Zaduo fault is revealed to be a strike-slip fault with some degree of thrust faulting based on the active tectonic map of China, which is consistent with the eastward extrusion of the Qiangtang block evidenced by GPS velocities (Fig. 1). Therefore, normal-slip events will probably not occur on the NW-trending Zaduo fault.

In addition, the Zaduo earthquake also indicates that the deformation of the Tibetan Plateau is occurring not only along the block boundaries but also within the blocks. Two alternative end-member models have been proposed to explain the deformation of the Tibetan Plateau. The block model suggests that major deformation occurs along major block-bounding faults, with minor faulting and little deformation occurring within the blocks (e.g., Armijo et al. 1989; Tapponnier et al. 2001). In contrast, the continuum model treats the lower crust of the Tibetan Plateau as a viscous sheet and suggests that the India–Eurasia collision is accommodated by the thickening of the lower crust and by broadly distributed

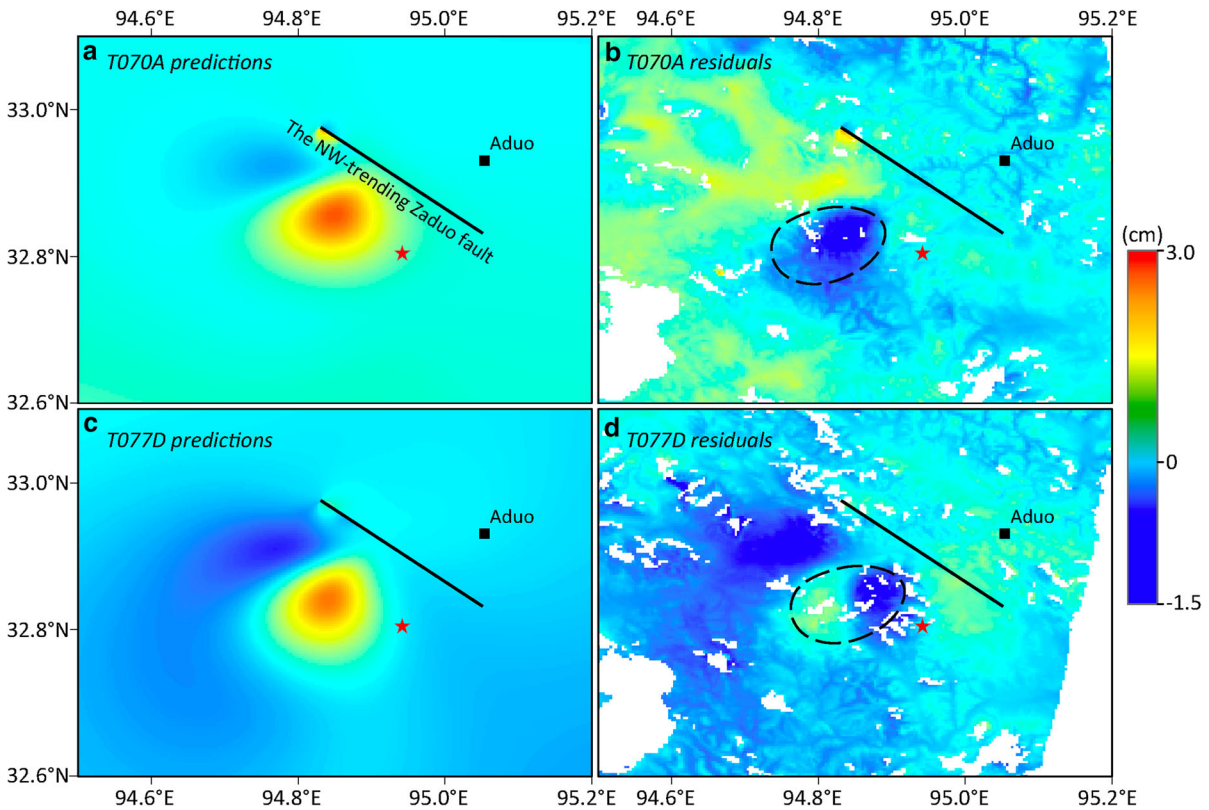

Figure 6

Fitting results of the NW-trending slip model to the two InSAR interferograms. **a**, **c** are the predicted LOS displacement maps for tracks T070A and T077D, respectively. **b**, **d** are the corresponding residual displacements. The black dashed lines outline regions with distinct residual displacements

deformation (e.g., England and Mckenzie 1982; Flesch et al. 2001). Thus, in the continuum model, the deformation within the blocks and along the boundaries is approximately equivalent. Therefore, quantification of deformation along block boundaries and within blocks is very important for discrimination between the two end-member models. For the regions lacking GPS observations, such as the center of the Qiangtang block, the slip magnitudes of historical earthquakes based on geodetic or geologic studies can provide robust evidences to identify the two end-member models.

6. Conclusions

We use Sentinel-1 InSAR-derived surface displacements to model the seismogenic fault and slip distribution of the 2016 Mw 5.9 Zaduo earthquake in Qinghai. Our results show that the NE-trending Aduo fault is responsible for this event. This fault had a distinct left-lateral strike-slip component before the late Tertiary. The normal-faulting feature of the Zaduo earthquake implies that the Qiangtang block probably consists of two or more sub-blocks with different eastward extrusion velocities. The Zaduo earthquake, with a peak slip of $\sim$ 31 cm, indicates that the deformation of the Qiangtang block is occurring not only along the block boundaries but also within the block. Our results provide further evidence for discrimination between the block and continuum end-member deformation models.

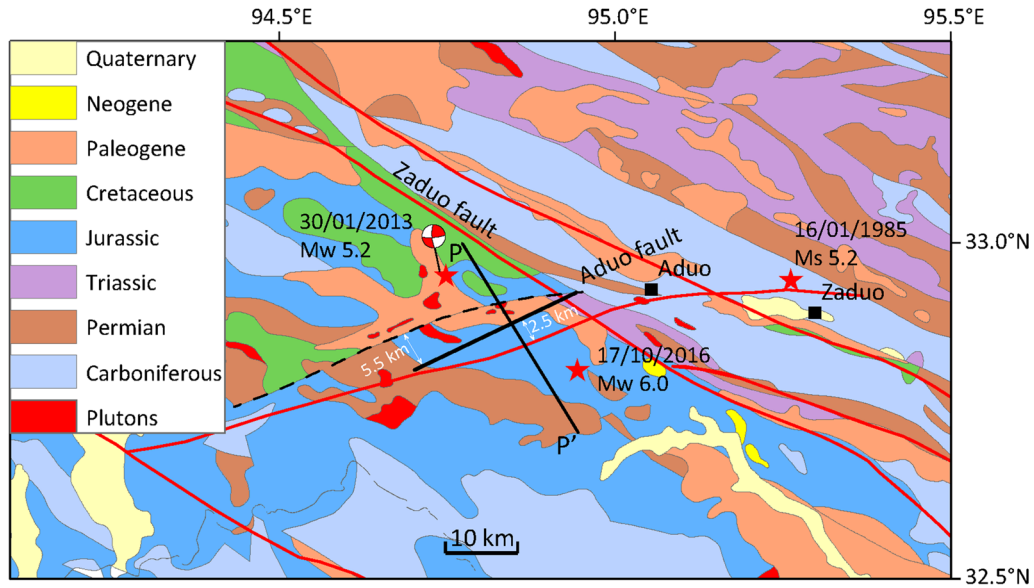

Figure 7
Geological map in the seismic region of the Zaduo earthquake. The dashed black line denotes the NE-trending fault revealed by the offset of strata. The black line is the modeled ruptured fault. The red lines are the known faults from the active tectonic map of China (Deng et al., 2007). Two $M > 5$ earthquakes were retrieved from the catalog of China Seismic Network (CSN) from 1970 to 2016. The focal mechanism of the 2013 M_w 5.2 earthquake was provided by GCMT

Acknowledgements

The authors thank the Editor and two anonymous reviewers for their constructive comments. The SAR images were obtained from the ESA Scientific Data Hub (https://scihub.esa.int). The geological map was obtained from the National Geological Archives of China (http://geodata.ngac.cn).

This study is supported by the Hong Kong Scholars Program, the National Natural Science Foundation of China (Nos. 41774011, 41721003, 41404012, and 4151101233), the National Earthquake Prediction Experiment Site in the Sichuan-Yunnan Region Program (No. 2017CESE0103), the Earthquake Monitoring and Forecasting Areas Project (No. 2018010103) and the National Key Basic Research Development Program (973 program) (Nos. 2013CB733304 and 2013CB733303).

References

Armijo, R., Tapponnier, P., & Tonglin, H. (1989). Late Cenozoic right lateral strike-slip faulting in southern Tibet. *Journal of Geophysical Research, 94,* 2787–2838.

Avouac, J. P., Meng, L., Wei, S., Wang, T., & Ampuero, J.-P. (2015). Lower edge of locked Main Himalayan Thrust unzipped by the 2015 Gorkha earthquake. *Nature Geoscience, 8,* 708–713.

Bell, J. W., Amelung, F., Ferretti, A., Bianchi, M., & Novali, F. (2008). Permanent scatterer InSAR reveals seasonal and long-term aquifer-system response to groundwater pumping and artificial recharge. *Water Resources Research, 44,* W02407. https://doi.org/10.1029/2007WR006152.

Bürgmann, R., Ayhan, M. E., Fielding, E. J., Wright, T. J., McClusky, S., Aktug, B., et al. (2002). Deformation during the 12 November 1999 Düzce, Turkey, earthquake from GPS and InSAR Data. *Bulletin of the Seismological Society of America, 92,* 161–171.

Deng, Q., Chang, Y., Hsu, K., & Fan, F. (1979). On the tectonic stress field in China and its relation to plate movement. *Physics of the Earth and Planetary Interiors, 18,* 257–273.

Deng, Q., Ran, Y., Yang, X., Min, W., & Chu, Q. (2007). *Map of Active Tectonics in China.* Beijing: Seimological Press.

Dziewonski, A. M., Chou, T.-A., & Woodhouse, J. H. (1981). Determination of earthquake source parameters from waveform data for studies of global and regional seismicity. *Journal of Geophysical Research, 86,* 2825–2852.

Ekström, G., Nettles, M., & Dziewonski, A. M. (2012). The global CMT project 2004-2010: Centroid-moment tensors for 13,017 earthquakes. *Physics of the Earth and Planetary Interiors, 200–201,* 1–9. https://doi.org/10.1016/j.pepi.2012.04.002.

England, P. C., & Houseman, G. A. (1989). Extension during continental convergence, with application to the Tibetan Plateau. *Journal of Geophysical Research, 94,* 17561–17579. https://doi.org/10.1029/JB094iB12p17561.

England, P., & McKenzie, D. (1982). A thin viscous sheet for continental deformation. *Geophysical Journal of the Royal Astronomical Society, 70,* 295–321.

Fang, L. H., Wu, J. P., Wang, W. L., Du, W. K., Su, J. R., Wang, C. Z., et al. (2015). Aftershock Observation and Analysis of the 2013 M_S 7.0 Lushan Earthquake. *Seismological Research Letters, 86*(4), 1135–1142. https://doi.org/10.1785/0220140186.

Farr, T., Rosen, P., & Caro, E. (2000). The shuttle radar topography mission. *Reviews of Geophysics, 45*(2), 37–55. https://doi.org/10.1029/2005RG000183.

Feng, W., Li, Z., Elliott, J. R., Fukushima, Y., Hoey, T., Singleton, A., et al. (2013). The 2011 M_w 6.8 Burma earthquake: Fault constraints provided by multiple SAR techniques. *Geophysical Journal International, 195,* 650–660.

Flesch, L. M., Haines, A. J., & Holt, W. E. (2001). Dynamics of the India-Eurasia collision zone. *Journal of Geophysical Research, 106,* 16435–16460.

Fujiwara, S., Nishimura, T., Murakami, M., Nakagawa, H., & Tobita, M. (2000). 2.5-D surface deformation of M 6.1 earthquake near Mt Iwate detected by SAR interferometry. *Geophysical Research Letter, 27,* 2049–2052.

Fujiwara, T., Kodaira, S., No, T., Kaiho, Y., Takahashi, N., & Kaneda, Y. (2011). The 2011 Tohoku-Oki earthquake: displacement reaching the trench axis. *Science*, *334*, 1240.

Fukahata, Y., & Wright, T. J. (2008). A non-linear geodetic data inversion using ABIC for slip distribution of a fault with an unknown dip angle. *Geophysical Journal International*, *173*, 353–364.

Funning, G. J., Parsons, B., Wright, T. J., Jackson, J. A., & Fielding, E. J. (2005). Surface displacements and source parameters of the 2003 Bam (Iran) earthquake from Envisat advanced synthetic aperture radar imagery. *Journal of Geophysical Research, 110,* B09406. https://doi.org/10.1029/2004JB003338.

Goldstein, R., & Werner, C. (1998). Radar interferogram filtering for geophysical applications. *Geophysical Research Letter, 25*(21), 4035–4038.

Goldstein, R., Zebker, H., & Werner, C. (1988). Satellite radar interferometry: Two-dimensional phase unwrapping. *Radio Science, 23*(4), 713–720.

Hanssen, R. F. (2001). *Radar Interferometry: Data interpretation and error analysis*. Dordrecht: Kluwer Academic Publishers.

Hooper, A., Zebker, H., Segall, P., & Kampes, B. (2004). A new method for measuring deformation on volcanoes and other natural terrains using InSAR persistent scatterers. *Geophysical Research Letters, 31,* L23611. https://doi.org/10.1029/2004GL021737.

Jiang, G., Wen, Y., Liu, Y., Xu, X., Fang, L., Chen, G., et al. (2015). Joint analysis of the 2014 Kangding, southwest China, earthquake sequence with seismicity relocation and InSAR inversion. *Geophysical Research Letter, 42,* 3273–3281. https://doi.org/10.1002/2015GL063750.

Jiang, G., Xu, C., Wen, Y., Liu, Y., Yin, Z., & Wang, J. (2013). Inversion for coseismic slip distribution of the 2010 Mw 6.9 Yushu earthquake from InSAR data using angular dislocations. *Geophysical Journal International, 194*(2), 1011–1022.

Jónsson, S., Zebker, H., Segall, P., & Amelung, F. (2002). Fault slip distribution of the 1999 M_w 7.1 Hector Mine, California, earthquake, estimated from satellite radar and GPS measurements. *Bulletin of the Seismological Society of America, 92,* 1377–1389.

Klein, F. W. (2002). User's guide to HYPOINVERSE-2000, a Fortran program to solve for earthquake locations & magnitudes. US Geological Survey.

Laske, G., Masters, G., Ma, Z., Pasyanos, M. (2013). Update on CRUST1.0—A 1-degree Global Model of Earth's Crust. Geophysical Research Abstracts 15. Abstract EGU2013-2658.

Liang, S., Gan, W., Shen, C., Xiao, G., Liu, J., Chen, W., et al. (2013). Three-dimensional velocity field of present-day crustal motion of the Tibetan Plateau derived from GPS measurements. *Journal of Geophysical Research: Solid Earth, 118,* 5722–5732. https://doi.org/10.1002/2013JB010503.

Liu, Y., Xu, C., Wen, Y., He, P., & Jiang, G. (2012). Fault rupture model of the 2008 Dangxiong (Tibet, China) M_w 6.3 earthquake from Envisat and ALOS data. *Advance Space Research, 50,* 952–962.

Massonnet, D., Rossi, M., Carmona, C., Adragna, F., Peltzer, G., Feigl, K. et al. (1993). The displacement field of the Landers earthquake mapped by radar interferometry. *Nature*, *364*, 138–142.

McCaffrey, R. (2005). Block kinematics of the Pacific-North America plate boundary in the southwestern United States from inversion of GPS, seismological, and geologic data. *Journal of Geophysical Research, 110,* B07401. https://doi.org/10.1029/2004JB003307.

Okada, Y. (1992). Internal deformation due to shear and tensile faults in a half-space. *Bulletin of the Seismological Society of America, 82*(2), 1018–1040.

Parsons, B., Wright, T. J., Rowe, P., Andrews, J., Jackson, J., Walker, R., et al. (2006). The 1994 Sefidabeh (eastern Iran) earthquakes revisited: New evidence from satellite radar interferometry and carbonate dating about the growth of an active fold above a blind thrust fault. *Geophysical Journal International, 164,* 202–217.

Resor, P. G. (2003). Deformation associated with continental normal faults. PhD dissertation, Stanford University.

Rubinstein, R. Y. (1981). *Simulation and the Monte Carlo Method. Wiley series in probability and mathematical statistics*. New York: Wiley.

Scheiber, R., & Moreira, A. (2000). Coregistration of interferometric SAR images using spectral diversity. *IEEE Transactions on Geoscience and Remote Sensing, 38*(5), 2179–2191.

Stark, P. B., & Parker, R. L. (1995). Bounded variable least squares: an algorithm and application. *Computational Statistics, 10,* 129–141.

Tapponier, P., & Molnar, P. (1977). Active faulting and tectonics in China. *Journal of Geophysical Research, 82,* 2905–2930.

Tapponnier, P., Xu, Z., Roger, F., Meyer, B., Arnaud, N., Wittlinger, G., et al. (2001). Oblique step-wise growth of the Tibetan Plateau. *Science, 294,* 1671–1677.

Waldhauser, F., & Ellsworth, W. L. (2000). A double-difference earthquake location algorithm: Method and application to the Northern Hayward fault, California. *Bulletin of the Seismological Society of America, 90,* 1353–1368.

Welstead, S. T. (1999). *Fractal and wavelet image compression techniques* (pp. 51–54). Washington: SPIE Optical Engineering Press.

Wen, Y., Xu, C., Liu, Y., & Jiang, G. (2016). Deformation and source parameters of the 2015 M_w 6.5 earthquake in Pishan, Western China, from Sentinel-1A and ALOS-2 data. *Remote Sensing, 8*(2), 134. https://doi.org/10.3390/rs8020134.

Werner, C., Wegmüller, U., Strozzi, T., Wiesmann, A. (2001). GAMMA SAR and interferometric processing software. Proceeding of ERS ENVISAT Symposium, Gothenburg, Sweden, 16–20 Oct.

Xu, C. J., Ding, K. H., Cai, J. Q., & Grafarend, E. W. (2009a). Methods of determining weight scaling factors for geodetic-geophysical joint inversion. *Journal of Geodynamics, 47,* 39–46.

Xu, W., Dutta, R., & Jónsson, S. (2015). Identifying active faults by improving earthquake locations with InSAR data and bayesian estimation: The 2004 Tabuk (Saudi Arabia) Earthquake Sequence. *Bulletin of the Seismological Society of America, 105*(2A), 765–775.

Xu, X., Wen, X., Yu, G., Chen, G., Klinger, Y., Hubbard, J., et al. (2009b). Coseismic reverse- and oblique-slip surface faulting generated by the 2008 M_w 7.9 Wenchuan earthquake, China. *Geology, 37*(6), 515–518.

Xu, C., Xu, B., Wen, Y., & Liu, Y. (2016). Heterogeneous fault mechanisms of the 6 October 2008 M_w 6.3 Dangxiong (Tibet) earthquake using Interferometric Synthetic Aperture Radar observations. *Remote Sensing, 8,* 228. https://doi.org/10.3390/rs8030228.

Xu, X., Yu, G., Klinger, Y., Tapponnier, P., & Van Der Woerd, J. (2006). Reevaluation of surface rupture parameters and faulting segmentation of the 2001 Kunlunshan earthquake (M_w 7.8), northern Tibetan Plateau, China. *Journal of Geophysical Research, 111,* B05316. https://doi.org/10.1029/2004JB003488.

Yu, C., Penna, N. T., & Li, Z. (2017). Generation of real-time mode high-resolution water vapor fields from GPS observations. *Journal of Geophysical Research, 122,* 2008–2025. https://doi.org/10.1002/2016JD025753.

Zhang, Y., & Zheng, J. (1994). *Geological overview in Kokshili, Qinghai and adjacent areas*. Beijing: China Seismological Press.

(Received February 16, 2018, revised June 28, 2018, accepted July 10, 2018, Published online July 27, 2018)